The *Anemomilos* prediction methodology for Dst

W. K. Tobiska,[1] D. Knipp,[1,2,3] W. J. Burke,[1] D. Bouwer,[1] J. Bailey,[1] D. Odstrcil,[1] M. P. Hagan,[1] J. Gannon,[4] and B. R. Bowman[5]

[1]   This paper describes new capabilities for operational geomagnetic D̲isturbance s̲torm t̲ime (Dst) index forecasts. We present a data-driven, deterministic algorithm called *Anemomilos* for forecasting Dst out to a maximum of 6 days for large, medium, and small storms, depending upon transit time to the Earth. This capability is used for operational satellite management and debris avoidance in Low Earth Orbit (LEO). *Anemomilos* has a 15 min cadence, 1 h time granularity, 144 h prediction window (+6 days), and up to 1 h latency. A new finding is that nearly all flare events above a certain irradiance threshold, occurring within a defined solar longitude/latitude region and having sufficient estimated liftoff velocity of ejected material, will produce a geoeffective Dst perturbation. Three solar observables are used for operational Dst forecasting: flare magnitude, integrated flare irradiance through time, and event location. Magnitude is a proxy for ejecta quantity or mass and, combined with speed derived from the integrated flare irradiance, represents the kinetic energy. Speed is estimated as the line-of-sight velocity for events within 45° radial of solar disk center. Storms resulting from high-speed streams emanating from coronal holes are not modeled or predicted. A new result is that solar disk, not limb, observable features are used for predictive techniques. Comparisons between *Anemomilos* predicted and measured Dst for every hour over 25 months in three continuous time frames between 2001 (high solar activity), 2005 (low solar activity), and 2012 (rising solar activity) are shown. The *Anemomilos* operational algorithm was developed for a specific customer use related to thermospheric mass density forecasting. It is an operational space weather technology breakthrough using solar disk observables to predict geomagnetically effective Dst up to several days at 1 h time granularity. Real-time forecasts are presented at http://sol.spacenvironment.net/~sam_ops/index.html?

1. Introduction

[2]   An ability to make short-term forecasts of solar energetic processes is important for operational space systems users. Forecasts of solar irradiances responsible for thermospheric low- and mid-latitude heating as well as of charged particles that lead to high-latitude heating are important for

[1]Space Environment Technologies, Space Weather Division, Pacific Palisades, California, USA.
[2]High Altitude Observatory, NCAR, Boulder, Colorado, USA.
[3]Aerospace Engineering Sciences, University of Colorado, Boulder, Colorado, USA.
[4]USGS Geomagnetism Program, Golden, Colorado, USA.
[5]U.S. Air Force Space Command/A9Y, Peterson Air Force Base, Colorado Springs, Colorado, USA.

Corresponding author: W. K. Tobiska, Space Environment Technologies, Space Weather Division, 1676 Palisades Dr., Pacific Palisades, CA 90272, USA. (ktobiska@spacewx.com)

thermospheric density models such as Jacchia-Bowman 2008 (JB2008) [*Bowman et al.*, 2008a, 2008b]. JB2008 provides accurate thermospheric mass densities useful for Low Earth Orbit (LEO) satellite orbital operations. Such forecasts typically support mission planning activities (hours-to-days) and executions of command (minutes-to-hours).

[3]   *Pre-event* probabilistic solar forecasts have been previously developed for solar flares and coronal mass ejections (CMEs) [e.g., *Barnes et al.*, 2007; *Falconer et al.*, 2011]. Solar flares are explosive releases of magnetic energy manifest in the solar atmosphere by sudden brightenings of electromagnetic radiation at hard X-rays through far ultraviolet (FUV) and visible to radio wavelengths. CMEs are inhomogeneous streams/clouds of energetic charged particles that escape from the solar atmosphere into the heliosphere. Probabilistic methods can improve the qualitative prediction for the occurrence of large, disruptive events at Earth.

[4]   *Event-driven* persistence and recurrence linear predictive solar irradiance forecasts have been used in operational solar irradiance forecasting [*Tobiska*, 2003; *Tobiska and Bouwer*, 2006] while statistical, neural network, or other techniques have been used for short-term (hours) geomagnetic

(Disturbance storm time index—Dst) forecasting [e.g., *Burton et al.*, 1975; *Valdivia et al.*, 1996; *Chen et al.*, 1997; *O'Brien and McPherron*, 2000; and *Temerin and Li*, 2002]. In this paper, we describe a new Dst prediction methodology called *Anemomilos* ("windmill" in Greek) that was developed for satellite operations; it is deterministic, data driven, and based on observable solar conditions.

[5] The *Anemomilos* methodology emerged from several insights while studying every hour of solar activity totaling two years during high, low, and rising solar cycle conditions:

[6] 1. the large majority of solar flare events above a certain irradiance magnitude threshold, within a defined solar longitude/latitude region with respect to the solar disk center and with sufficient speed, produce a Dst event;

[7] 2. solar flare irradiance magnitude, integrated flare irradiance, and erupting event location can be specified with the regularity and cadence needed for operational users; and

[8] 3. solar eruptive events can produce separate, different types of magnetized solar emissions, e.g., CMEs, high-speed streams, or small-scale ejecta; these can merge on their way to Earth and, through superposition, produce a longer or larger Dst event than would be anticipated if these events arrived separately with longer temporal separation.

[9] We describe below the observed/specified solar physical mechanisms and the methodology for predicting a Dst geomagnetic event, which can be applied to many uses.

2. Operational Dst Forecast Advancements

[10] Community efforts in recent years have improved forecasts of solar wind events. Solar flares and CMEs drive these events that affect Earth's nearby space environment and our society's technological systems. For example, ENLIL/Cone/Wang-Sheeley-Arge (WSA) is a hybrid system of physics-based and empirical models that characterizes solar wind parameters; it has been implemented both at NOAA's Space Weather Prediction Center (SWPC) [*Pizzo et al.*, 2011] and at NASA's Community Coordinated Modeling Center (CCMC).

[11] Additionally, the U.S. Air Force (USAF) has sponsored other research-to-operations work to bridge the "valley-of-death" for transition of models into operations; a particular focus has been to capture solar wind effects that impact the terrestrial magnetosphere and generate severe space weather. Near Earth, these space weather events disrupt orbits for thousands of objects, especially those in Low Earth Orbit (LEO). We report on the recently completed USAF-sponsored research for the *Operational Real-time and Forecast USGS Dst* project. This project was funded between 2009 and 2012 under the Small Business Innovative Research (SBIR) program. Recently, *Lanzerotti* [2012] identified the emerging growth of small businesses and their progress in making an impact on the space weather enterprise with new products. One example of that progress is the result of this SBIR work, which has produced a continuous, fully redundant data stream of real-time and forecast Dst useful for operations; it uses multiple Dst data sources (http://sol.spaceenvironment.net/~maps/). The project, called

Magnetospheric Alert and Prediction System (MAPS), also developed the *Anemomilos* methodology to forecast up to 6 days. Its real-time results are at http://sol.spaceenvironment.net/~sam_ops/index.html?.

[12] The motivation for USAF support of the MAPS SBIR is that accurate specification and forecast of thermospheric densities for LEO satellite orbit calculations are required. The JB2008 thermospheric density model [*Bowman et al.*, 2008a, 2008b; *Tobiska et al.*, 2008] is used to provide high accuracy mass densities for satellite operators. This model uses the Dst index as a proxy to characterize the energy input at high latitudes during geomagnetic storms. In addition to providing an operational, real-time, fully redundant Dst data stream, the second goal of MAPS was to provide an accurate Dst forecast with time granularity of 3 h, a 72 h prediction window, and a 3 h latency. That capability was developed, demonstrated, exceeded, and implemented at a Technology Readiness Level (TRL) 9 in February 2013. TRL 9 is defined by an ISO standard [ISO 16290, 2012] as "the mission objectives, operational environment and performance requirements are established and agreed upon by the stakeholders; the capability is mature following successful operation and performance achievement in an actual operational environment." The resulting capabilities are 15 min cadence, 1 h time granularity, 144 h prediction window, and up to 1 h latency. The *Anemomilos* Dst forecast capability described below is sometimes called "data Stream B" by operational users; it is intended to be a system-level back-up for the ENLIL/Cone/WSA "data Stream A" capability.

[13] We remind the reader that the complete set of physical processes of the coupled Sun-Earth system are not described here, such as how magnetic energy is input into an active region to create a flare and erupting flux rope or how the ejecta in the Interplanetary Magnetic Field (IMF) couples with the magnetosphere to create a disturbance to the Earth main magnetic field. The *Anemomilos* Dst forecast capability does not aim to replace physics-based models like those running at CCMC, the USAF Space Weather Operations Center, or the NOAA Space Weather Prediction Center. Examples are the Potential Field Source Surface (PFSS) [*Luhmann et al.*, 2002; *Altschuler and Newkirk*, 1969; *Hoeksema*, 1984; *Schatten et al.*, 1969; *Wang and Sheeley*, 1992], CORHEL [*Lionello et al.*, 2001; *Riley et al.*, 2001, 2002; *Mikic et al.*, 1999], WSA [*Arge and Pizzo*, 2000], ENLIL [*Odstrčil and Pizzo*, 1999; *Odstrcil et al.*, 2004; *Emmons et al.*, 2013], HAF [*Fry et al.*, 2001, 2003], SWMF [*Tóth et al.*, 2005], LFM [*Lyon et al.*, 2004; *Merkin and Lyon*, 2010], OpenGGCM [*Raeder et al.*, 2001], RCM [*Toffoletto et al.*, 2003; *Wolf et al.*, 1991], or Tsyganenko [*Tsyganenko and Sitnov*, 2005, 2007], for example. Instead, it provides a specific operational capability using a redundant forecasting methodology for thermospheric density specification. We assume, a priori, that physical processes occur to create charged particle ejecta at the Sun, release it into the IMF, and then transit to Earth where coupling with the Earth's magnetosphere occurs to create a geomagnetic disturbance reported as Dst. *Anemomilos* also does not model or predict storms resulting from high-speed streams that

have their origin in coronal holes, nor from the fraction of CMEs that erupt from disappearing filaments without an associated flare. These storms can be severe but the physical processes behind them are not represented in *Anemomilos*.

3. The Disturbance Storm Time Index, Dst

[14] When heated plasma is ejected from the Sun into the magnetized solar wind, the resulting inhomogeneous clouds often contain structures whose properties differ from those normally encountered in quiescent interplanetary space. Multidirectional magnetic polarity particle clusters (sometime organized as magnetic clouds with a slowly rotating magnetic field) may support large solar wind density perturbations and drive shocks if their speeds are high relative to the background solar wind. If the structures arrive at Earth, they can generate geomagnetic storms that are temporary but major disturbances within the Earth's magnetosphere-ionosphere-thermosphere (M-I-T) system. These disturbances are caused by changes in the solar wind densities, velocities, and pressures as well as in the polarity and magnetic (**B**) field magnitude of the IMF. These structures interact with the Earth's magnetospheric magnetic field to produce large perturbations in Earth's main magnetic field and are measured as well as reported by ground magnetic observatories as local and planetary geomagnetic indices.

[15] The Dst index is one of those geomagnetic indices and it is used to estimate the globally averaged changes in the horizontal component of the Earth's main magnetic field (ΔH) using measurements from four off-equatorial magnetic observatories. It is unique in that the electric currents responsible for Dst are diverse and can reside far from Earth on the magnetopause, in the magnetotail, and in the magnetospheric ring current. The latter source, for example, acts to depress the total strength of the main magnetic field at the Earth's surface. Other magnetic indices such as the auroral electrojet (*AE*) index represent responses to currents flowing in the Earth's ionosphere.

[16] Geomagnetic storms are typically defined by three phase changes in the Dst index: *initial*, *main*, and *recovery*. If solar wind pressure persists for some duration of time, then the initial impulse is called an initial phase, where Dst is positive and relatively steady. Specifically, the initial phase often begins with a storm sudden commencement (SSC) characterized by sharp (+10 to +50 nT) increases in the horizontal ($\Delta H > 0$) component of the Earth's field in time scales that can be less than 10 min. The SSC is commonly associated with an increase in the dynamic pressure of the solar wind. The initial phase may continue for up to several hours with positive ΔH. Not all geomagnetic storms have a prolonged initial phase and not all sudden increases in Dst are followed by geomagnetic storms.

[17] A geomagnetic storm's main phase is defined by a significant decrease in Dst with time. At the Earth's surface during a storm, low-latitude magnetic signatures are often asymmetric in local time. This is associated with a number of physical processes, including partial ring currents, partially connected field-aligned currents with circuits through the ionosphere, and partially connected currents from the magnetotail to the inner magnetosphere and then to the magnetopause [*Love and Gannon*, 2010]. A threshold for declaration of a storm varies by forecasting agency and by customer sensitivity. For example, NOAA SWPC's G-scale uses the following conventions: G1 (Kp = 5 minor storm); G2 (Kp = 6 moderate storm); G3 (Kp = 7 strong storm); G4 (Kp = 8 severe storm); and G5 (Kp = 9 extreme storm). JB2008 uses the Dst index to estimate storm time thermospheric densities whenever it falls below −75 nT; otherwise, the coarser ap index is used. The minimum value during a storm is often between −50 and −600 nT and the duration of the main phase can extend from 1 h to more than 12 h. The Dst relaxes from its minimum value back towards its quiet time value during the recovery phase, which may last for several days during large events.

3.1. Dst Usage in Space Weather Operations

[18] Dst is used as a proxy for characterizing the effects of charged particle ejecta embedded in the solar wind, sometimes referred to as magnetized solar emissions. These produce diverse effects at Earth when interacting both with the M-I-T natural environment and with our technological systems. Because it is often useful to know when and where operational systems become susceptible to storm-related effects, Dst provides a convenient proxy with its time-resolved initiation, main, and recovery phase time frames. The USGS Dst, for example, has 1 min time-resolved values. This time resolution, its operational availability, and the existence of a long-term historical database were the main reasons why Dst was selected as a proxy for high-latitude heating in the JB2008 thermospheric density model. Figure 1 shows space weather timescales related to satellite activities where historical, real-time, and forecast Dst would be relevant to postanalysis, maneuver decision or planning, and reentry update activities, as an example.

[19] In addition to the changes in thermosphere densities that are important for satellite operations, geomagnetic storms cause enhanced particle fluxes at Geosynchronous Earth Orbit (GEO) and Medium Earth Orbit (MEO); those can, in turn, lead to surface and internal spacecraft charging with a resulting failure of spacecraft electronics components. For example, a fast solar wind with high particle fluxes and a Bz southward IMF can drive polar convection patterns that destabilize ionospheric plasma resulting in degraded radar signal propagation, disrupted radio communications, lost GPS signals, and elevated ground induced currents (GICs), the latter of which impact electric power station operations. However, without a sustained period of Bz southward IMF, the effects may not reach the lower latitude regions sufficiently to affect Dst. Dst is used as a proxy for identifying potential impacts in these areas.

[20] During severe space weather events, solar flares and CMEs can produce relativistic solar energetic particles (SEPs) that directly modulate the radiation environment from deep space, GEO, MEO, and LEO down to the Earth's tropospheric lower atmosphere. For example, Galactic Cosmic Rays (GCRs) provide a tissue- and silicon-relevant
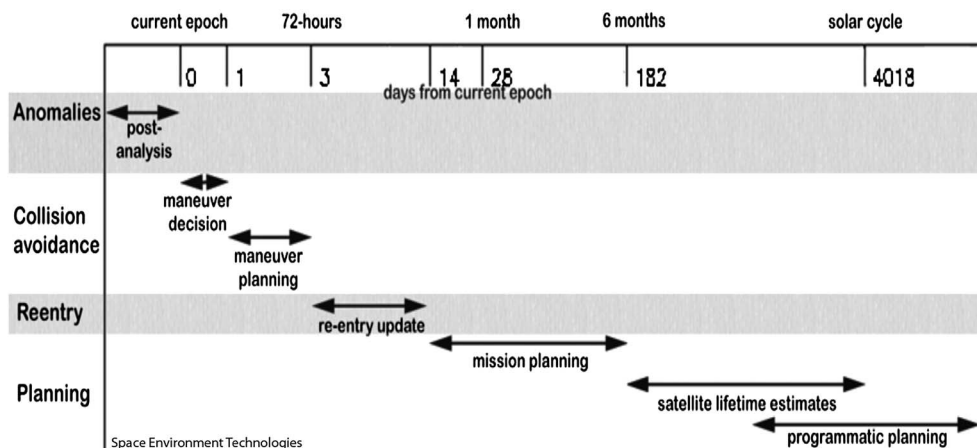
Figure 1. Timescales of satellite activities related to space weather.

radiation dose rate background that maximizes in the strato-sphere (20–25 km or 60,000–80,000 ft., called the Pfotzer Maximum) that varies inversely with the solar cycle. Upon this slowly changing background, SEP events additionally increase the radiation risk in air/space travel for commercial crew, frequent flyers, fetuses, space tourists, and astronauts. The location of penetration through the atmosphere of these solar energetic particles is also dependent, in part, upon magnetic cutoff rigidities that vary with the strength and configuration of the magnetospheric magnetic field. Dst helps characterize the state of the magnetosphere for obtaining a better estimate of the radiation dose rate envi-ronment as an input into the Tsyganenko Geomagnetic Field Model [*Tsyganenko and Sitnov*, 2007] used by the NASA Nowcast of Atmospheric Ionizing Radiation System (NAIRAS) [*Mertens et al.*, 2009].

3.2. Real-Time Dst

[21] Dst (*Sugiura and Hendricks*, 1967; *Mayaud*, 1980) is pro-vided operationally for real-time and recent historical use by the Kyoto World Data Center (Kyoto) (http://wdc.kugi.kyoto-u.ac.jp/dst_realtime/—described in the next para-graph in more detail), the U.S. Geological Survey (USGS) (http://geomag.usgs.gov), Space Environment Corporation (SEC) (http://www.spacenv.com), Atmospheric and Environ-mental Research (AER) (http://www.aer.com/dst), and Space Environment Technologies (SET) (http://sol.spacenvironment.net/~maps/). Kyoto, SEC, and USGS estimate their Dst based on the four standard ground magnetometer obser-vatories operated by three national agencies: Hermanus (HER), South Africa (South African National Space Agency); Kakioka (KAK), Japan (Japan Meteorological Agency); Honolulu (HON), Hawaii (U.S. Geological Survey); and
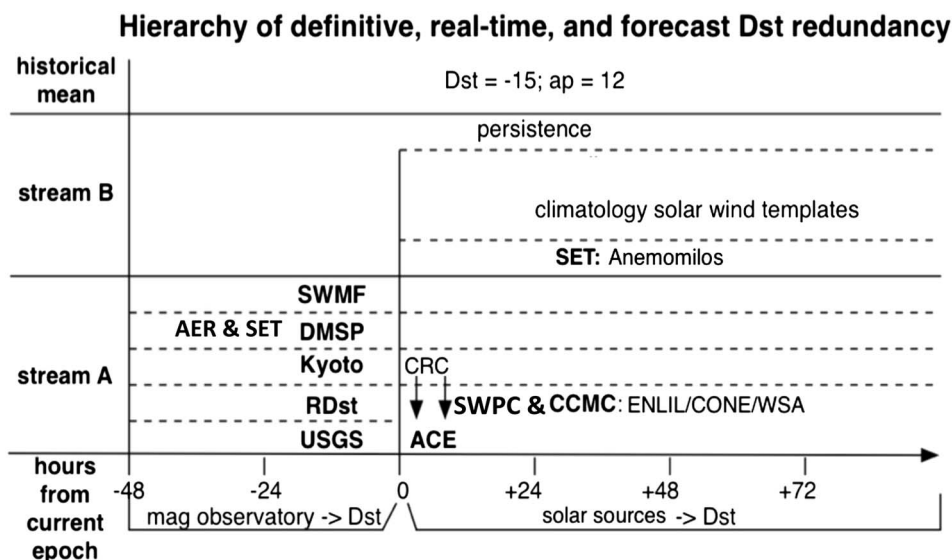
Figure 2. Institutional Dst products listed by time frame versus data stream.

SanJuan (SJG), Puerto Rico (U.S. Geological Survey). AER and SET produce a Dst using the Defense Meteorological Satellite Program (DMSP) satellite data. In addition, NASA CCMC creates a real-time modeled Dst based on the Bats-R-Us model and a ring current model with the Space Weather Modeling Framework (SWMF) developed at the University of Michigan. Figure 2 shows institutional Dst products listed by time frame versus data stream.

[22] It should be noted that the real-time WDC Kyoto Dst data stream discussed here is actually the Kyoto quick-look Dst and is the defacto standard used by the world. Those data are accessed publicly at http://wdc.kugi.kyoto-u.ac.jp/. The Kyoto quick-look file is updated every hour and retrieved by SET. The historical (provisional) Kyoto Dst has a large delay in posting to the Kyoto site because of delays in processing the data with a baseline correction. The provisional Dst is located at http://wdc.kugi.kyoto-u.ac.jp/dst_provisional/index-j.html and their near real-time Dst is at http://wdc.kugi.kyoto-u.ac.jp/dst_realtime/index.html. The difference between provisional Dst and final Dst is normally 5–10 nT. The difference between real-time (quick-look) Dst and provisional (or final) Dst is sometimes very large. However, it is usually corrected after a few days with revised data and the difference may be similar with the case of provisional Dst. SET automatically updates the Kyoto Dst database when revised data become available.

3.3. Forecast Redundancy

[23] SET's operational forecasts use the *Anemomilos* Dst algorithm as a back-up, stream B data source. Carmel Research Center (CRC) (http://www.carmelresearchcenter.com) produces a forecast Dst as do other organizations such as Rice University Space Institute (RSI) (http://mms.rice.edu/realtime/forecast.html) and University of Colorado Laboratory for Atmospheric and Space Physics (UCB LASP). Future (stream A) Dst algorithms are being derived from the ENLIL/Cone/WSA system (http://www.swpc.noaa.gov/wsa-enlil/) operated by NOAA SWPC and, alternatively, by the NASA CCMC iSWA system (http://iswa.ccmc.gsfc.nasa.gov/IswaSystemWebApp/). In this paper, we discuss the basis, development, and validation of only the *Anemomilos* algorithm.

[24] Figure 2 shows the institutions that create Dst products that can be used for operations as a function of the data stream to which the product belongs. Data streams are an important part of an operational system design that addresses data outage risks through the use of redundancy. To mitigate an operational risk that data will be unavailable to end users, the concept of a *data stream flow* is employed. There are at least two data streams "flowing" through an operational system; algorithms recognize a data object as belonging to either a primary "A" (enhanced) or secondary "B" (climatology) data stream. The primary "A" data stream contains enhanced data by virtue of its finer time resolution, spatial detail, physics-based fidelity, or reduced uncertainty. The drawback is that, for a variety of reasons, some data sets may become unavailable. The secondary "B" data stream contains core data that are fundamental

for maintaining space weather climatology information flow. This type of information stream is usually easier to produce and, while the uncertainties may be larger, it still represents a valid data solution. By using two streams in parallel with each other, with one taking primacy, the measured (past or current) or modeled (current or future) data have a much greater probability of being available. The redundant data stream attribute is a major design feature of the entire system employed by SET and all data objects belong to either the "A" or "B" streams. In the event of data outages, the penalty is a graceful degradation of the end product with greater uncertainty, less time resolution, or longer latency but not a catastrophic failure to deliver.

4. Operational Basis for *Anemomilos*

[25] A multidecade debate about the relationship between CMEs and flares has revealed that these phenomena are related to magnetic reconnection but are not causally related to each other. Nonetheless, there is a close association between energetic flares and CMEs. Flare-CME relationships have been studied by *Kahler* [1992], *Gosling* [1993], *Harrison* [1995], *Zhang et al.* [2001], *Yashiro et al.* [2006], *Chen and Zong* [2009], *Yashiro and Gopalswamy* [2009], *Jain et al.* [2010], *Chen and Kunkel* [2010], *Bak-Steslicka et al.* [2013], *Bhatt et al.* [2013], and many others.

[26] *Jain et al.* [2010] showed that the speed of CMEs increases with the plasma temperature of X-ray flares, having a correlation coefficient $r = 0.82$. When energy fluence rates exceed 10^{-1} J m^{-2}, *Yashiro and Gopalswamy* [2009] reported nearly a one-to-one correspondence between flares and CMEs. These studies suggest that there should be a way to incorporate information from GOES satellite X-ray flare measurements into a geomagnetic storm forecasting algorithm. The underpinning of the *Anemomilos* algorithm is a presumed relationship between the magnitude, integrated irradiance, and location of CME-associated flares and subsequent geomagnetic storms at Earth.

[27] Our work, based on the study of 259 flare/Dst pairs during high, declining, and rising solar cycle activity, and covering more than 18,000 observation hours totaling more than two years, enabled us to take the more general flare-CME relationship and move it into an operational paradigm. During the intervals that we studied at the suggestion of our customer (15 January to 15 July 2001; 1 March to 28 September 2005; and 1 December 2011 to 30 November 2012), nearly every energetic flare event above a certain irradiance threshold, described below, was *deterministically* related to a Dst event. This surprising relationship allowed us to create an algorithm with sufficient robustness to be incorporated into an operational forecasting routine that eventually forecasts neutral densities in the thermosphere, i.e., JB2008. A summary of the operational basis of *Anemomilos* and its relationship to physical processes is useful as a short introduction. The forecasting considerations are size, speed, and location for a magnetic eruptive event to intercept Earth.
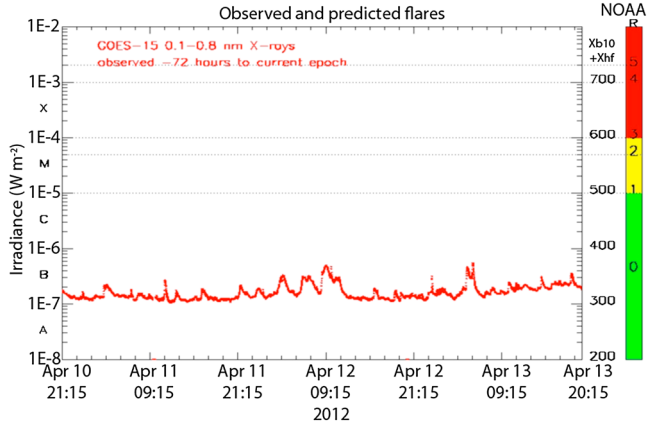
Figure 3. GOES 0.1–0.8 nm flux. Note that "predicted flares" in the figure title refers to an ability of this SET algorithm to forecast an evolution of a flare once it occurs (not prediction). No events of this type are shown in this figure.

4.1. Size

[28] *Aarnio et al.* [2011] used CMEs with well-measured masses from the LASCO CME database and flares with optical counterpart positions from the GOES flare database to calibrate a relationship between solar flare flux and CME mass. They found over 800 candidate flare-CME pairs that met the criteria of (1) a CME occurring within 10–80 min after a flare and (2) that CME occurring within ±45° in position angle of the flare on the solar disk. For CMEs associated with flares, they reported that the stronger the associated flare, the more massive the CME. They also found the width of a flare-associated CME to be directly correlated with the flux of the flare, with X-class flare-associated CMEs being the widest (80° ± 10°) and B-class flare-associated CMEs the most narrow (42° ± 1.4°). *Yashiro et al.* [2006] show a clear correlation between increasingly energetic flares, in terms of X-ray flux, and the appearance of associated CMEs. *Yashiro and Gopalswamy* [2009] report that flares with X-ray flux at the 5×10^{-5} W m^{-2} irradiance level are associated with CME eruptions approximately 60% of the time. This level corresponds to a GOES X-ray Spectrometer (XRS) M5.5 flare or NOAA Radio Blackout Storm Scale G2 shown in Figure 3. Further, they found that a fluence of 10^{-1} J m^{-2} is associated with CME eruptions approximately 80% of the time. Similarly, *Bak-Steslicka et al.* [2013] report that the parameters of the long duration event flares (GOES XRS flux and duration of the rising phase) show strong correlations with the CME parameters of velocity, acceleration during main acceleration phase, and duration of the CME acceleration phase. This relation between CMEs and with long duration events (LDEs) is another indicator that flare fluence may be an important forecast parameter. Clearly the associations are not perfect and many of the associations have wide spreads of uncertainty. As we discuss in below, for our forecasting purposes, we use a flux background removal method to improve upon the statistics for the flare-CME relationship.

4.2. Speed

[29] The *Anemomilos* algorithm uses an empirically derived Sun-to-Earth speed that we believe corresponds roughly to a combination of: (1) the *Chen and Kunkel* [2010] relation between rate of injection of magnetic flux into an erupting flux rope or CME, the integrated GOES soft X-ray (XUV or SXR) emission, and the acceleration, a, of the flux rope out of the corona; (2) the kinematic description of CME motion in *Vršnak et al.* [2004]; and (3) the flare-flux CME-deceleration relationship discussed in *Aarnio et al.* [2011]. The *Anemomilos* algorithm attempts to encapsulate these results.

4.3. Location

[30] Regarding location, we find a zone of effectiveness on the solar disk that accounts for most of the significant Dst events at Earth. Figures 4 and 5 show how the location of the *Anemomilos* flare events (see discussion below for information on the color coding) is related to the observed Dst magnitude at Earth for the 259 flare-Dst pairs we studied. Figure 4 shows all the paired flare-Dst events in traditional heliocentric Mercator coordinates with the center-of-disk marked by a circle/cross. Figure 5 shows all the paired events in polar plot coordinates; both plots have the solar obliquity angle corrected as described below. The Figure 5 radial angle from the disk center is used in *Anemomilos* as a discriminator to test whether or not an event has the potential to be geoeffective based on location. Most of the geoeffective events are within ±45° on the heliographic subsolar point. The Dst event relative size of small ($-34 < \mathrm{Dst} \leq 0$ nT), medium ($-159 < \mathrm{Dst} \leq -34$ nT), or large ($\mathrm{Dst} \leq -159$ nT) is graphically represented by the size of the dot. An observable for establishing the Sun-Earth ejecta connection is a solar disk-derived proxy of the centroid of a flare's location. Real-time (5 min cadence and 5 min latency) image data from NASA's Solar Dynamics Observatory (SDO) geosynchronous satellite provide this flare location information. See details below.
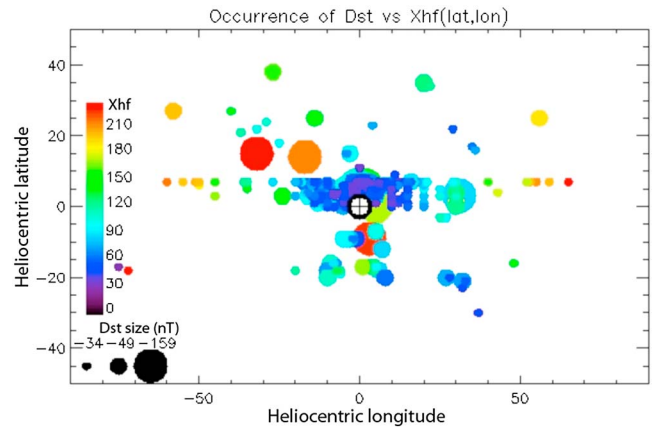

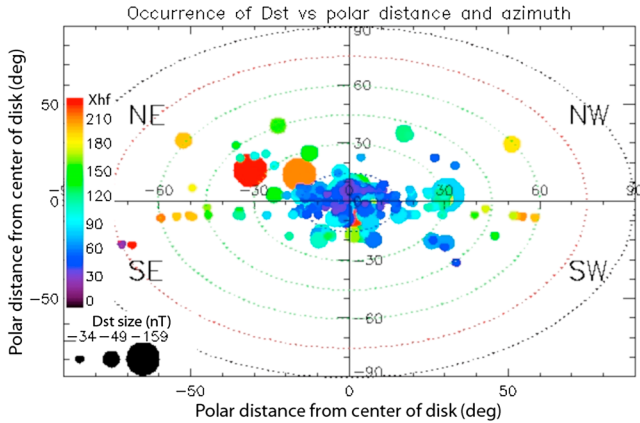**Figure 4.** All Xhf-Dst pairs for 2001, 2005, and 2012 Mercator projection.

Figure 5. All Xhf-Dst pairs (2001, 2005, and 2012) sub-Earth polar projection.

4.4. X-ray Flux as Proxy for Magnitude of Dst Response

[31] Solar flares are identified in the GOES XRS 0.1–0.8 nm band, available with 1 min time resolution (Figure 3). NASA's SDO EUV Variability Experiment (EVE) produces an XRS surrogate in the event that the GOES XRS data stream is offline. In an operational (automated) setting, we find that it is important to distinguish between the X-ray irradiance background and the flare event. During very active times, emissions from individual flares are convolved with the emissions from nonflaring bright active regions in X-ray data time series. Thus, a magnitude X-class flare on the NOAA scale may actually be from a region producing a smaller M-class flare if the flare occurs in addition to an ensemble of emission background from across the solar disk or from active limb emission. In other words, many nonflare bright regions within the GOES field of view can contribute to the flare signal.

[32] To alleviate this problem, and to isolate the unique magnitude of each flaring event, SET developed the unitless daily X-ray background (Xb10) (Figure 6 lower panel) and hourly Xhf (Figure 6 upper panel) indices [*Tobiska and Bouwer*, 2006]. The Xb10 index is used to establish an irradiance baseline. The remaining Xhf index with the baseline removed is an indicator of the past hour's flare values and is updated every 5 min. We employ the hourly Xhf to quantify, then relate, solar flare activity to assumed solar charged particle ejecta and ultimately to Dst disturbances. There is a threshold, Xhf = 40, below which we do not forecast Dst events. Above this threshold, we scale a statistical Dst template to small, medium, and large sizes based on the Dst value during the main phase; the scaling has been empirically determined based on our study of the 2001 and 2005 data located in Appendix A. Figure 6 shows the Xhf and Xb10 time series for early 2012. The large flare events in March 2012 were associated with Xb10 values of ~375 and Xhf values of ~250. Figure 5 shows all occurrences of Xhf events in intervals of 2001, 2005, and 2012 used in this study. The magnitude of

Xhf is represented by the dot color ranging from blue (Xhf = 40) to red (Xhf >210).

[33] The information in Figures 4–6 is empirically encapsulated in the *Anemomilos* algorithm as the basis for forecasting small, medium, or large Dst events at Earth. *Anemomilos* uses a statistical Dst storm profile that derives from a composite template for Dst events observed by the USGS during solar cycle 23 [*Gannon*, 2012]. The USGS composite Dst storm profile contains initial, main, and recovery phases; an example is shown in Figure 7 as the blue line. *Anemomilos* uses a scaled USGS template for Dst sizes of small, medium, and large events based on the Xhf index and location, described above, and the integrated irradiance hour flare index, Xhf, that is related to speed and described below.

4.5. Integrated Irradiance X-ray Flare Index, Xhf, as a Proxy Ejecta Speed

[34] The Earth arrival timing for the ejected solar plasma is critical if one is to obtain an accurate Dst magnitude change and morphology. We empirically derived a radial velocity (line-of-sight speed) for events within 45° radially of the solar disk center. It is based on the integrated flare magnitude, i.e., the integrated value of the Xhf flare index, and is consistent with previous theoretical work [*Chen and Kunkel*, 2010]. We find that a temporal integration of the Xhf value provides a good proxy for the speed of the ejecta in its transit from the Sun to Earth. Thus, the integral of Xhf (IX) provides crucial information regarding the start of a Dst event initial phase.

[35] Mass leaving the Sun during eruptive events is generally associated with flux rope ejections. The ejecta are often modeled as force-free erupting flux ropes (EFRs) that undergo dramatic expansion and changes in acceleration within a small number of solar radii posteruption [*Chen*, 1996]. The EFRs have been described by many authors [e.g., *Chen*, 1996; *Shimojo and Shibata*, 2000; *Reames*,
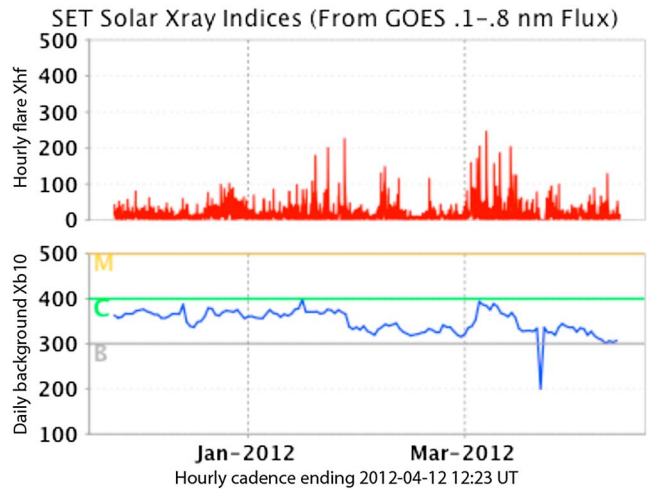

Figure 6. Daily Xb10 (lower panel) and hourly Xhf (upper panel) indices produced by SET from GOES XRS data.
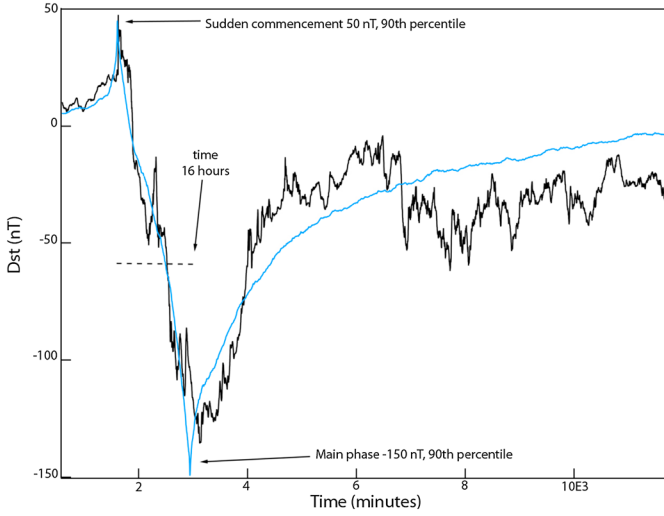
Figure 7. USGS composite Dst (blue line) compared with an actual event but derived from cycle 23 data.

2002; *Török and Kliem*, 2005; *NASA/TM—2006–214137*, 2006, and *Chen and Kunkel*, 2010] and are acted upon by a combination of forces, e.g., Lorentz, gravity, and drag.

[36] *Chen and Kunkel* [2010] investigated a range of flare/CME events and found a temporal and physical connection between coronal mass ejections and flares. They treated flares and CMEs as separate manifestations of the same energetic process whereby poloidal magnetic flux was injected into the toroidal flux ropes. They found that flare brightness, due to accelerating particles, was proportional to the strength of the electrodynamics of the magnetic flux injection into the flux rope. They considered the XUV GOES light curves for B-, C-, and M-class limb flares and their associated CME trajectories determined from SOHO LASCO and STEREO/SECCHI images. Their study established a relationship between the theoretical rate of injection of magnetic flux, $d\varphi_p(t)/dt$, into an erupting flux rope, the integrated GOES XUV emission, and the acceleration, a, of the flux rope out of the corona and into the interplanetary medium. This relationship is expressed in equation (1) as

$$a \approx \frac{d\phi_p(t)}{dt} \qquad (1)$$

[37] For one GOES B-class flare event in 2008, they were able to follow the subsequent deceleration in the interplanetary medium. The peak speed of the ejecta was 1400 km s^{-1} near the Sun and over the course of 24 h the ejecta decelerated to a speed just above 500 km s^{-1}.

[38] Our study independently found a similar relationship between the integrated GOES XRS 0.1–0.8 nm light curve from eruptive events on the solar disk (not limb) and Dst events. Below, we describe a relationship between an empirically derived line-of-sight ejecta speed and GOES XRS integrated measurements; later we show how

the ensemble of these observations can be used operationally to create a forecast of Dst geoeffectiveness for events within 45° radially of the solar disk center.

[39] The speed of the ejecta was first calculated for our 2001 test period by identifying flaring events and their locations in SOHO Extreme ultraviolet Imaging Telescope (EIT) images, associating them with Xhf index values at the same epoch, then finding the most probable Dst perturbation created by each event. SOHO EIT images were often not available during a specific event; as a result, we used only those eruptive events where we could unambiguously determine the flare location and Xhf-Dst pair association for a Dst occurrence of any size. We also selected events that were close to the solar equator in order to maximize ecliptic plane effectiveness as well as restricted events to 45° radial from the disk center to ensure the validity of a line-of-sight velocity approximation. The combination of these restrictions resulted in a small sampling but it still allowed us to calculate a rough time-of-flight for each ejecta event from the Sun to Earth.

[40] These constraints resulted in a reduced set of 35 events that are shown in Figure 8; a subset (11 events in 2001) from these is shown in Table 1. Their speed was considered a total average speed for liftoff from the Sun, transit through the IPM, and arrival at Earth. The ensemble of these identified events provided a means to derive velocity from integrated Xhf; they are shown as the points closest to the linear regression blue line in Figure 8. Other points close to the regression line were not part of the 2001 derivation set. There are also several data points considerably off the line and these are events that had slower or faster velocities than those calculated from the 2005 and 2012 time periods. Error in estimating velocity can occur from unknown geometry of flux ropes, ejecta source regions being on the edge of IMF lines connected to the Earth, unresolved accelerations at ejecta liftoff, or unknown causes for velocities changes (e.g., shock interactions) while the material is in transit to Earth.

[41] We note that a solution to the problem of velocity uncertainty is to incorporate observations of this material
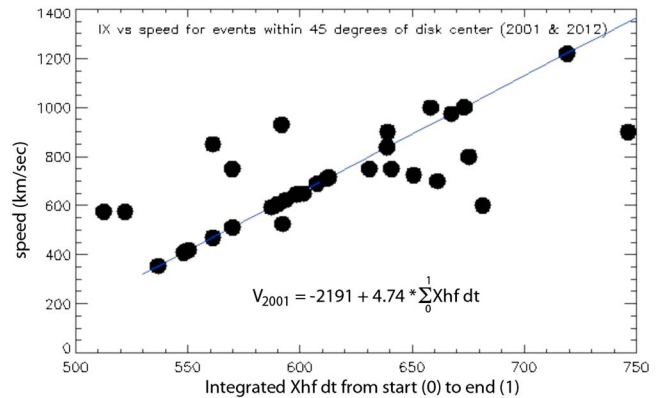

Figure 8. Derived speed from integrated Xhf (IX). Eleven points close to the regression line are the 2001 values used to derive the relationship.

Table 1. Dst-Related Events Used in Integrated Xhf-Speed Derivation

Use	Flare Date	Xhf	∫Xhf/dt	Speed[a]	Lat/Lon[b]	R[c]	Az[d]
Derivation	200103161050	67	569.9	511	N00W02	7	15
	200103170436	84	561.1	469	N00E20	21	−70
	200103170641	52	607.6	690	N00W01	7	8
	200103180756	43	550.3	418	N00W02	7	15
	200103200227	64	598.9	649	N00E02	7	−15
	200103201515	66	612.9	715	N00E16	17	−65
	200103292110	47	593.5	623	N00W07	9	49
	200104090426	84	673.2	1001	S15E03	9	−161
	200104120027	97	612.0	711	N00W25	25	78
	200104160714	57	548.1	408	N00W15	15	71
	200104250521	43	590.3	608	N00E01	4	−14
Validation	201204181518	62	536.8	354	S26W33	38	125
	201204181719	77	587.2	593	S26W32	37	125
	201205092111	103	638.7	838	N15E25	30	−52
	201206141553	102	719.1	1219	S19E06	19	−163

[a]Speed in km s^{-1}.
[b]Heliocentric latitude and longitude in degrees (°) from heliocentric disk center.
[c]Radius in degrees (°) from disk center (sub-Earth point) with solar obliquity angle applied.
[d]Azimuth in degrees (°) from solar North (West = 90°) with solar obliquity angle applied.

during its inner heliosphere passage and the Interplanetary Scintillation (IPS) methodology holds promise for providing that type of observation to correct the in-transit velocities. IPS observations are line-of-sight-integrated observations through the solar wind to distant galactic radio sources that may contain smearing in the data, i.e., an ambiguity in determining where, along a line of sight, the observed signal originates. Researchers use a tomographic technique to disentangle this line-of-sight smearing where both solar rotation and outward motion of structures in the solar wind over time provide views from different perspectives that are required for a tomographic analysis [*Jackson et al.*, 1998].

[42] The linear regression equation used in this work to create an average ejecta velocity is described below and is reprinted in Figure 8. In Figure 8, "IX" refers to the Integrated Xhf. The blue line is the relationship derived from the 11 events in the 2001 data period and those regression coefficients are now used operationally.

[43] We tested our derived velocities against all available data. There were a total of 259 flare eruption/Dst associated pair events and these are identified in Appendix A. The listing in Appendix A of the Xhf-Dst paired events provides the UT time (YYYYMMDDhhmm), Xhf value, a magnitude class for Xhf (similar, but not identical, NOAA X-ray flare classes), speed (km s^{-1}), solar flare event location (heliocentric latitude and longitude), obliquity angle corrected latitude Lat*, radius, and azimuth from solar sub-Earth point where Az is N = 0, W = 90, S = 180 or −180, E = −90, and Dst size. Eleven derivation and four example events are listed as the shaded rows in Appendix A. The entire data set has a range from 194 to 3000 km s^{-1}, a median ejecta transit speed of 750 km s^{-1}, and a mean of 779 km s^{-1}.

[44] For operations, *Anemomilos* uses two methods for estimating speed. First, when there is no other ability to obtain speed, e.g., the existence of an ambiguity in, or undetermined, Xhf start/stop times, then 750 km s^{-1} (the median speed in our data set) is used as the default value

for estimating the ejecta time-of-arrival at Earth. Second, if all operational information is available at the given epoch, that is, if the SDO EVE Solar Aspect Monitor (SAM) location data matches the GOES XRS Xhf timing within a few minutes to declare an event has been observed, then a derived speed can be calculated based on the Xhf integrated time. The Xhf integrated time is the start-to-end of the flare event. The event start is defined as the beginning of the GOES XRS 0.1–0.8 nm light curve rise above background and the event end is defined as the time where the irradiance values are one half the flare peak value compared to the background at the start of the event.

[45] The empirically derived speed-integrated Xhf relationship is

$$V = -2191 + 4.74 \int_0^1 Xhf\,dt \qquad (2)$$

where V is the ejecta's line-of-sight velocity [km/s], Xhf is the dimensionless flare index, $_0$ and $_1$ are start and stop times of the flare event, and dt is the length of the time for the event in seconds. This linear regression was based on the subset of 11 events that occurred in 2001 and shown in Table 1 and Figure 8.

[46] In support of our methodology that relates flare brightness to speed from solar disk observations, we note that *Zhang et al.* [2001] found a limb CME-speed relationship with integrated GOES soft X-ray flux measurements. Their study predated, but was similar to, the conclusions of *Chen and Kunkel* [2010] and they also indicated that flare-induced thermal pressure was not the cause of the CMEs but that flares and CMEs were two manifestations of the same magnetic process.

[47] The Xhf value is an excellent indicator of the flare magnitude and its integration over time serves as a proxy for acceleration. This is similar to the electromotive force associated with the flux injection that destabilizes and ejects
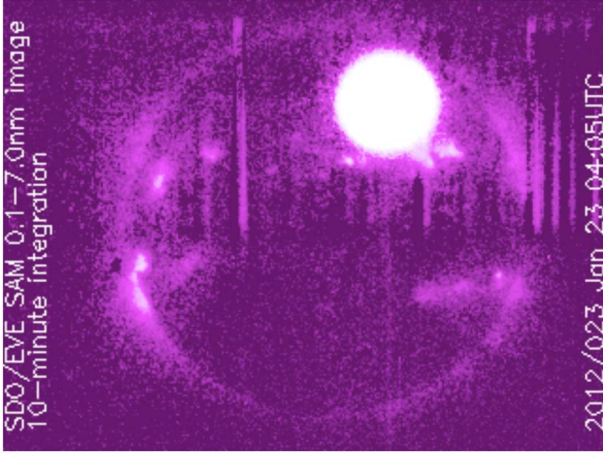
Figure 9. SAM detector image shows a bright flare event on 23 January 2012. The centroid of the bright event provides latitude/longitude location information.

the flux rope as described by *Chen and Kunkel* [2010]. Thus, the kinematic acceleration of the ejecta through an interval of time results in a velocity; the relationship is only strictly valid for line-of-sight velocity (speed) of events observed near disk center but in operations we use this for all events. In practice, most of the geoeffective events only occur near the disk center and are not limb events. If we assume that there is a constant velocity offset, c_1 (km s^{-1}), to correct for unknown total deceleration in the IMF and an acceleration multiplier, c_2 (km s^{-2}), that incorporates all the *Chen and Kunkel* [2010] main and residual ejecta liftoff acceleration terms, then equation (3) helps us understand the gross kinematics of equation (1) and the empirical relationship of equation (2)

$$v_1 = at_1 = c_1 + c_2 \int_0^1 Xhf dt \qquad (3)$$

[48] Here, the observationally determined linear regression constants for the Dst-effective Xhf events occurring near the center of solar disk are $c_1 = -2191$ km s^{-1} and $c_2 = 4.74$ km s^{-2} where v_1 is the average velocity at the Earth, a is the average acceleration between the Sun and Earth, and t_1 is the arrival time at Earth.

[49] For every hour of the 12 months of December 2011 through November 2012, we observed the Xhf, derived a velocity, found an integrated Xhf, determined an event location, and estimated a Dst event timing and magnitude. This 2012 period was used for operationally testing of our 2001 and 2005 development parameters and, based on this test period, we established the deterministic geoeffectiveness of flaring events as observed in Dst.

[50] Figure 4 shows all the paired events in traditional heliocentric Mercator coordinates with the center-of-disk marked by a circle/cross. Figure 5 shows all the paired events in polar plot coordinates; both plots have the solar obliquity angle corrected as discussed below. The Figure 5 radial angle

from the disk center is used in *Anemomilos* as a discriminator to test whether or not an event has the potential for geoeffectivity based on location. The Dst relative event size of small ($-34 <$ Dst ≤ 0 nT), medium ($-159 <$ Dst ≤ -34 nT), or large (Dst ≤ -159 nT) is graphically represented by the size of the dot. The magnitude of Xhf is represented by the dot color ranging from blue (Xhf $= 40$) to red (Xhf > 210).

4.6. Location as a Proxy for IMF Connectivity to Earth
4.6.1. SDO EVE SAM Data

[51] The proxy for IMF connectivity is the location of the erupting event on the solar disk; it can be identified by the centroid of brightness for the solar flare in heliocentric latitude and longitude. Imagery of flaring X-ray events must be obtained from satellites outside the atmosphere since X-rays are absorbed in the lower terrestrial thermosphere or mesosphere and do not reach the Earth's surface. NASA's SDO EVE SAM detector began operations in 2011 and has a 10 s observing cadence with a latency of less than 5 min to the ground. SAM operates on the principle of a pinhole camera and is sensitive to much of the same X-ray flare emissions observed by the GOES XRS 0.1–0.8 nm channel. The University of Colorado Laboratory for Atmospheric and Space Physics (LASP) team provides a space weather data product that is the centroid of the brightest SAM detector pixels reported in heliocentric latitude and longitude. During an operational run, the SAM bright centroid is associated with the X-ray flaring event (Figure 9). SET compares the event timing of the SAM centroid location with the Xhf index to determine an X-ray event's location for use by *Anemomilos*. The GOES Solar X-ray Imager (SXI) also produces a similar wavelength image of X-ray emissions and could be used for operationally determining the centroid of an eruptive event.

4.6.2. Heliocentric Latitude and Longitude as Well as the Solar Obliquity Angle

[52] The *Anemomilos* algorithm was developed for heliocentric longitude and latitude, as well as Xhf magnitude, and association of solar flares to geoeffective Dst. As a simplification, the empirical relationship was assumed to
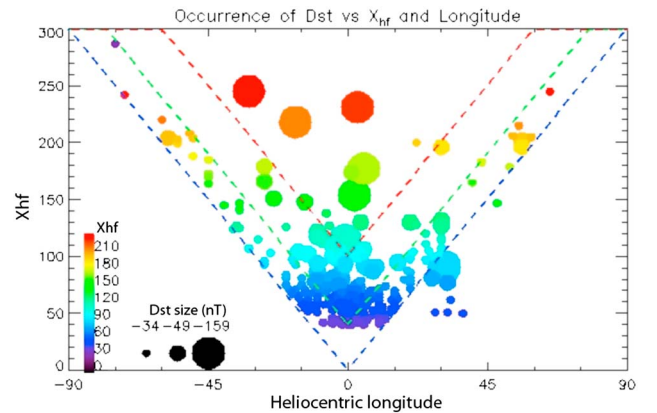

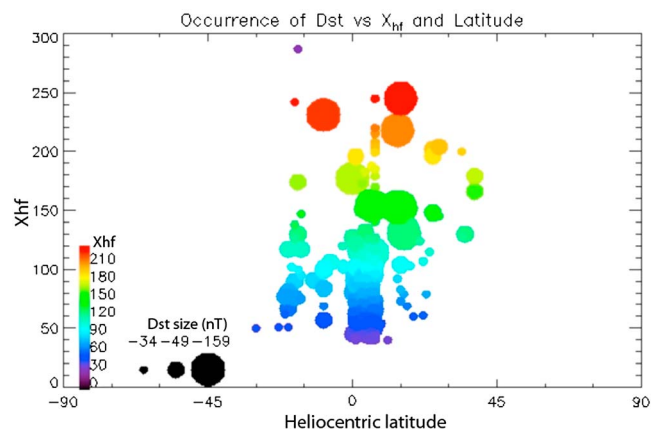**Figure 10.** Correspondence of Dst vs Xhf magnitude by solar longitude.

Figure 11. Correspondence of Dst vs Xhf magnitude by solar latitude.

be nearly linear starting with small magnitude events, e.g., Xhf in a range of 40 to 50, that could be geoeffective if they occurred within a few degrees of the sub-Earth point but ineffective if they occurred further away. Likewise, larger Xhf events, e.g., Xhf >100, could still be geoeffective toward the solar limbs at mid-latitudes (Figures 4 and 5). An empirical scaling factor was developed that reduced geoeffectiveness, i.e., magnitude of Dst, the further away from the center of disk an event occurred. This was based on the assumption that most EFR material coming from locations nearer the limb was inserted onto non-Earth directed IMF lines.

[53] Our data have been organized to show their latitude and longitude relationships with Xhf and Dst size. Figure 10 shows the dual dependency of the Dst magnitude on the Xhf combined with heliocentric longitude. Figure 11 shows the observed relationship between Dst magnitude, Xhf, and heliocentric latitude. Dashed lines in Figure 10 show the operationally defined envelope of effectiveness; above the lines solar eruptive events have a relationship with Dst, and below the lines there are generally no relationships. A notable exception in longitude space, Figure 10, is the set of small Xhf events that are located in the longitudes out to approximately W40°. This subset of small, southern hemisphere events appears to be correlated with Parker spiral IMF lines that intersect the Earth and that favor small eruptive events. We don't have enough data yet to determine if there is a generalized effect with northern hemisphere events as well.

[54] Our first study of these location relationships occurred during algorithm development for the 2001 and 2005 time frames in the maximum and decline of solar cycle 23. X-ray flaring locations associated with active regions occurred mostly at heliocentric latitudes between ±20° in those periods. All relevant SOHO EIT 30.4 and 28.4 nm images for the 2001 and 2005 time frames were reviewed to estimate event locations.

[55] The emergence of equatorial active regions that produce complex topography and that are associated with flares during the maximum and decline phases of a solar cycle is a result of the equatorward drift of active latitudes

as seen in the daily solar sunspot area butterfly diagram (Figure 12). Our data (Figure 5) were taken from 2001, 2005, and 2012 (Figure 12 vertical dashed lines), i.e., during different parts of the solar cycle. The 2001 and 2005 events tended to occur at lower latitudes during high and low solar activity, respectively, and the 2012 events tended to occur at higher latitudes up to ±40° during solar cycle rise from the minimum of the previous cycle toward maximum of cycle 24.

[56] In higher latitude events, ejected material may be inserted onto IMF lines that extend out of the ecliptic plane where most of their energy content could miss the Earth. This may have been partially the case for both the 20–22 January 2012 and 7–8 March 2012 flare events; they deserve further analysis with physics-based models. Figure 13 (Joe Allen, private communication, 2002) demonstrates the long-term effect of this, i.e., the peak of geomagnetic activity tends to lag the peak of the sunspot cycle. From the peak of a solar cycle to its decline, more of the active regions move to lower latitudes, in general, and this enables them to deposit their energy more often in the ecliptic plane, thus making them more geoeffective. Since there appears to be a rather sensitive latitude band above which a given event is not geoeffective, and below which it is, we must take the Earth-relative (ecliptic plane) position of the erupting event into account using the solar obliquity angle. Figure 14 shows that since the solar equator varies with respect to the ecliptic plane (the solar obliquity angle), and since solar flare event locations are provided in heliocentric coordinates, we must make an additional small correction to the latitudinal location of an event by applying the solar obliquity angle on a given date.

4.7. Southward Bz and Other Issues

[57] The *Anemomilos* algorithm does not contain an explicit IMF relationship. It is challenging to understand the performance of our simplified approach to geomagnetic
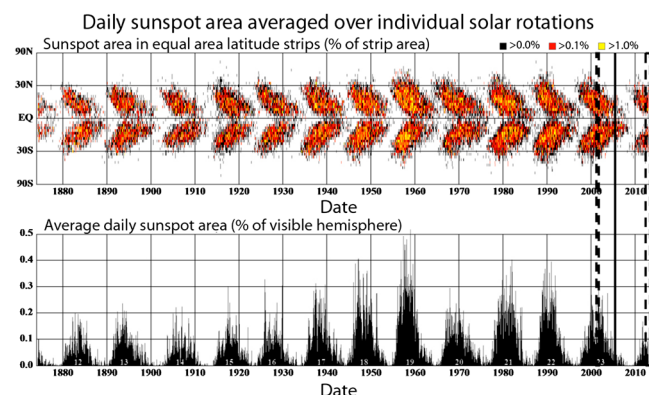

Figure 12. (Top panel) Daily solar sunspot area butterfly diagram and (lower panel) average daily sunspot area (credit D. Hathaway at NASA MSFC; images are at http://solarscience.msfc.nasa.gov/images/bfly.gif). Dashed vertical lines indicate the 2001, 2005, and 2012 data periods used in this study.
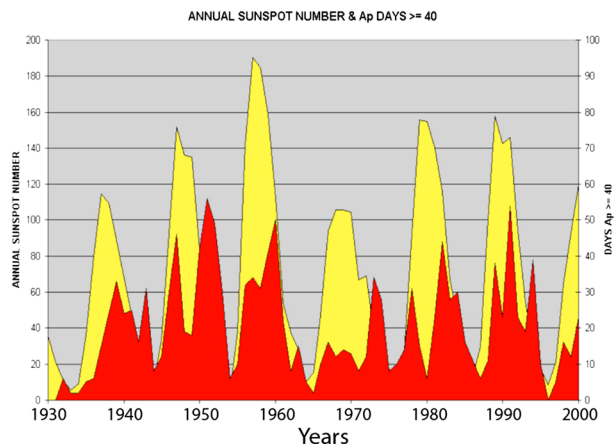
Figure 13. Solar cycles and geomagnetic storms (credit J. Allen).

storm forecasting as we were struck by the overall success of *Anemomilos* without using an observed Bz. We believe that there are two aspects of the method and its application that are important. The first is related to the likelihood of southward IMF during the passage of any given ejecta from the Sun to the Earth; the second is the relative role of southward IMF during storm processes.

[58] Most ejecta have intervals of southward IMF. *Mulligan et al.* [1998] discussed two types of idealized magnetic flux ropes that could pass Earth, i.e., magnetic flux ropes in the ecliptic that produce bipolar magnetic clouds and those tipped 90° with respect to the ecliptic that produce unipolar magnetic clouds. Magnetic flux ropes lying in the ecliptic have southward IMF either at the leading or trailing edge. Half of the highly inclined magnetic flux ropes should have southward IMF in their axial field. Thus, for idealized magnetic clouds at least 75% should contain intervals of southward IMF. Only about one third of all ejecta are magnetic clouds. The remaining two thirds of ejecta have "rougher" magnetic profiles that usually have at least some short intervals of southward IMF. Further, fast CMEs often drive shocks with enhanced IMF, which may point southward and thus initiate geospace storm processes even before the main body of the CME arrives. We suspect that our simplified forecasting approach is simply taking advantage of the likelihood that southward IMF is present in fast solar wind transients that pass Earth.

[59] The importance of southward IMF cannot be denied, but it is not the only factor in geomagnetic storm strength. Since *Dungey's* [1961] groundbreaking work on solar wind interaction with the Earth's magnetosphere, numerous studies have shown that southward IMF is the dominant factor in controlling energy input to geospace. The role of southward IMF was captured in the relationship known as the Akasofu epsilon coupling function that relates the solar wind IMF to the convective electric field [*Perreault and Akasofu*, 1978]. *Newell et al.* [2007] reviewed solar wind coupling processes and produced a new "universal coupling function," which places a strong emphasis on solar wind speed.

[60] Recent studies have shown that there is more to the coupling processes than can be explained by a single coupling function. *Borovsky and Denton* [2006] suggested that cold dense plasma, in the form of plasmaspheric drainage plumes from the inner magnetosphere, could be set into motion when the convective electric field increases abruptly. If this circulating plasma comes in contact the dayside reconnection site, the efficiency of solar wind-magnetospheric coupling is observed to decrease. Thus, processes other than direct solar wind interaction may be at work during storm time. In global simulations with a southward IMF, *Lopez et al.* [2010] showed that for large enough IMF strengths, the geoeffectiveness is not proportional to the field because the field convects around the magnetosphere instead of being reconnected. Additionally *Knipp et al.* [2011 and references therein] and *Li et al.* [2011] report that the east-west interplanetary field (IMF By) can dominate energy input to the dayside ionosphere-thermosphere system.

[61] We have not solved the issue of IMF orientation but hopefully these types of studies can offer more insight. Other questions were also raised in this regard: (a) perhaps B_Z is important for larger CME events but not for smaller ones; (b) we note that the superposition of multiple small events can create moderately large Dst activity, which may have been interpreted as a southward Bz effect in some cases; (c) perhaps if there is a By component of any significance, it may provide coupling paths to the magnetosphere in almost all cases except where Bz is almost entirely northward; (d) the coupling between speed, size, and Bz is an avenue for future study outside this empirical algorithm; and (e) the dominant orientation of the IMF may have a solar cycle dependency as noted by *Mulligan et al.* [1998] and our *Anemomilos* derivation with solar cycle 23 data may not be entirely accurate for solar cycle 24.

[62] Additionally, *Anemomilos* does not take into account corotating interaction regions (CIRs) or HSS. CIRs, while not eruptive events, are sourced in the open field lines emanating from coronal holes and can induce Dst disturbances on the order of a small substorm for a prolonged
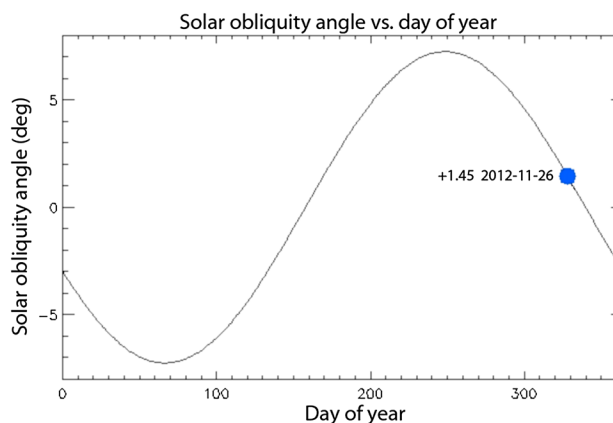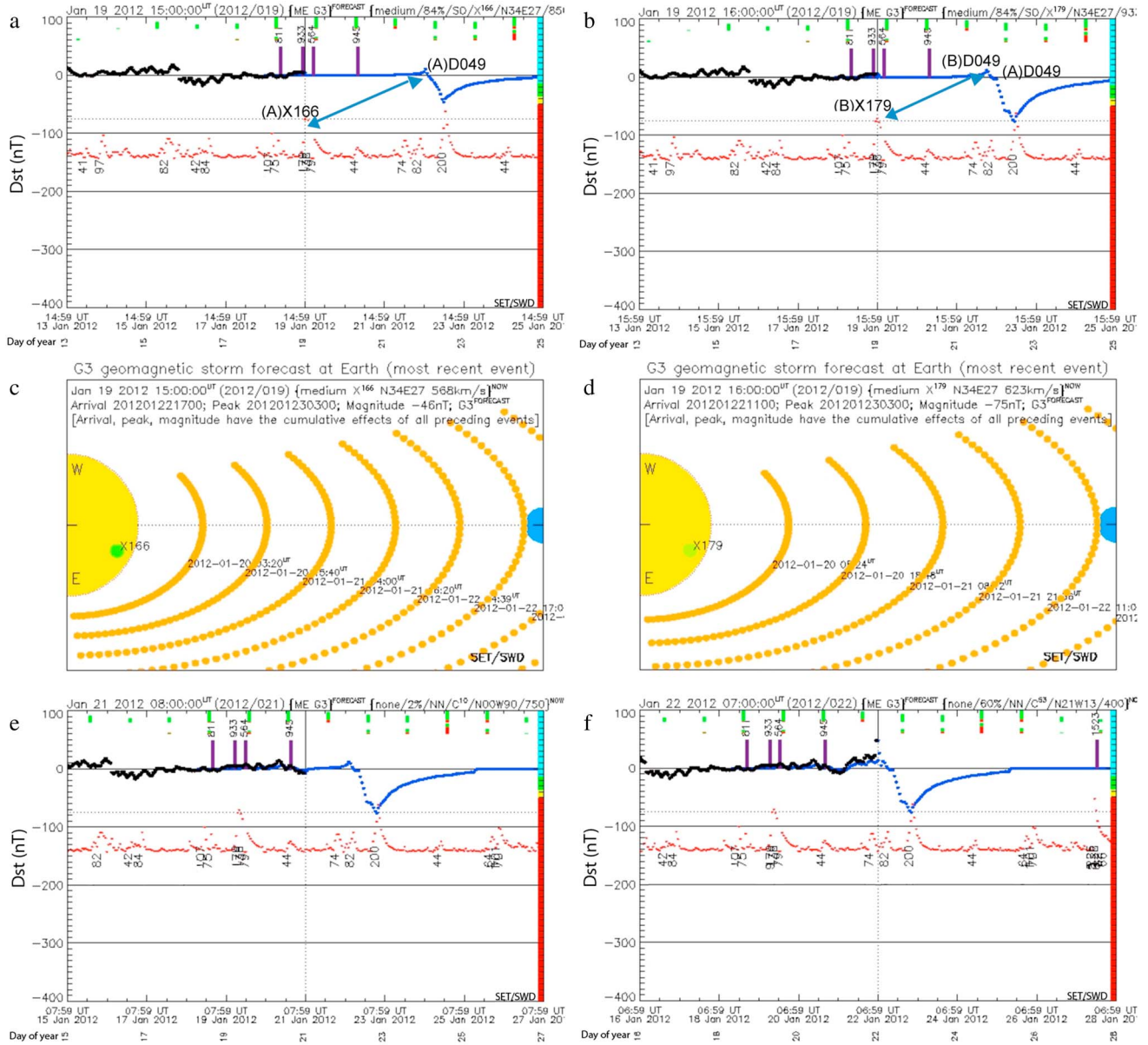

Figure 14. Solar obliquity angle.

Figure 15. (a) The first Xhf event (AX166) resulting in Dst event (AD-49). (b) The second Xhf event (BX179) resulting in Dst event (BD-49). (c) Event AX166 arrival as AD-49. (d) Event BX179 arrival as BD-49. (e) Combined enroute events. (f) Dst event BD-49 SSC arrival. (g) Storm main phase minimum. (h) The third Xhf event (CM200) resulting in Dst event (CD-34). (i) Dst event CD-34 SSC arrival. (j) End Dst recovery—all events.

period of time. We anticipate improving the algorithm with CIRs and HSS in the future.

[63] We have seen cases in our event list where very large solar limb events or greatly elongated moderate-sized midlongitude events may discharge a fraction of their plasma onto IMF lines that intersect the Earth even though the bulk of the material is not Earth directed. The algorithm does not distinguish the extent of the plasma on and off Earth-directed field lines or the geometry of EFRs; thus,

some events may be missed while others are overstated in magnitude.

[64] Finally, knowledge of the speed of the ejecta is critical to accurately estimate superposition of events and their timing; we believe our calculation of speed can be refined. If plasma is not ejected with most of the velocity component based on the line-of-sight assumption, the algorithm may overestimate the impact of the event; fortunately, smaller events that are geoeffective are also relatively close
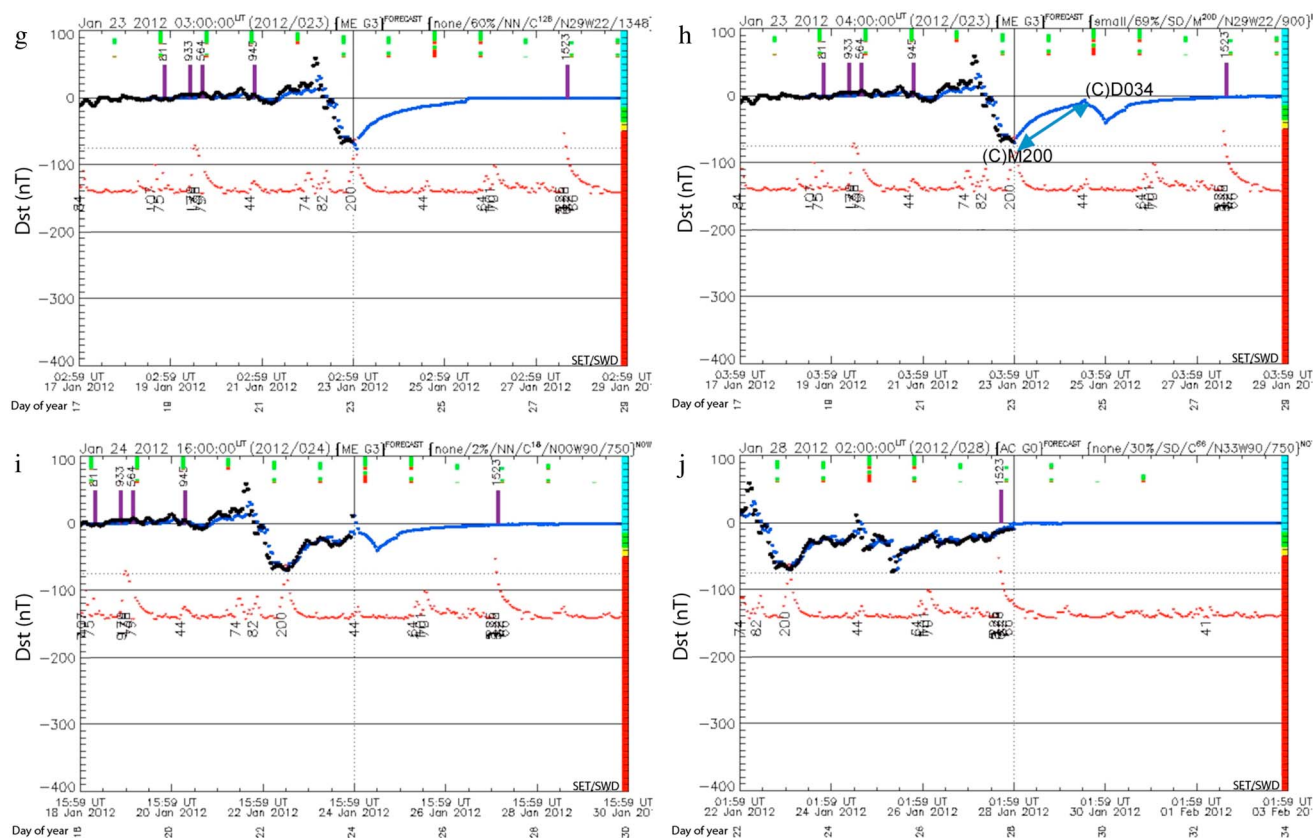
Figure 15. (continued)

to the center of the solar disk and this maintains the validity of the assumption.

[65] Improvements to *Anemomilos* are anticipated and will focus on: (i) an IMF **B** specification to obtain better Dst magnitudes, e.g., perhaps through IPS observations; (ii) the effects of CIRs and HSS; (iii) asymmetric plasma discharges onto Earth-directed and non-Earth-directed IMF lines and EFR geometry; and (iv) refined knowledge of ejecta speeds.

4.8. An *Anemomilos* Example

[66] An example of the *Anemomilos* forecast using the operational observables (flare magnitude, integrated flare irradiance, and location) is shown for 2012 in Figures 15a–15j. This is a period in late January 2012 when a series of medium-sized solar flare events occurred starting on 19 January around 1500 UT and centered at N34E27. While this was a particularly clear example, nearly all the events we studied had a similar forecast evolution and we show Figures 15a–15j that are representative of the *Anemomilos* capability. A movie example for the entire 2001 study period is available on YouTube at http://youtu.be/snxgoQ_s0o0.

[67] In these figures, the blue dots are the 1 h predicted Dst from *Anemomilos* and the black dots are the 1 h Kyoto Dst reported values (*y* axis scale); the red dots are the 1 h Xhf value (arbitrarily scaled for viewing and not related to

the *y* axis). All three are shown on the same UT time *x* axis with the time and date plus the day-of-year reported. The vertical dotted line is the current epoch, which is listed in the first set of figure title items as UT hours plus year and day-of-year.

[68] The second set of figure title items includes two pieces of information (superscript FORECAST) related to the predicted state for the most severe Dst based on all the combined future conditions, postcurrent epoch. The first two-character set describes the predicted size of the Dst event and is labeled as AC (All Clear), SE (Small Event), ME (Medium Event), or LE (Large Event) for Dst. The second two-character set is the NOAA G-scale prediction. Other plotted information that may exist in the real-time figures includes NOAA reported M5 – X10 flare class (labeled along a gold vertical bar above the Xhf values) and the NOAA reported Type II radio burst velocities (labeled along a purple vertical bar above the 0 nT line). The two red and/or green vertical bars above 60 nT are the daily solar flare probabilities (top bar, SP) and geomagnetic activity probabilities (bottom bar, GP) for the next 24 h. These are reported from the NOAA daily *Report of Solar Geophysical Activity* (RSGA) and plotted. SP green indicates an M5-class flare probability and red indicates an X1-class flare probability where the length of the colored bar is the relative probability on a 1% – 99% scale. GP green indicates

Table 2. Dst Forecast to Actual Comparisons for Jan–Jul 2001

IDX	HR	NowMean	NowSTD	0DyMean	0DySTD	1DyMean	1DySTD	2DyMean	2DySTD	3DyMean	3DySTD
2001	00	0.995	1.001	1	1.024	0.995	1.003	0.905	0.83	0.599	0.532
2001	12	0.996	1.001	0.991	1.013	0.993	1.011	0.934	0.957	0.593	0.513

a minor storm (Kp = 5) probability and red indicates a major storm (Kp ≥ 6) probability where the length of the colored bar is the relative probability on a 1% – 99% scale. All NOAA information is provided for informational purposes only and is not used in the *Anemomilos* Dst forecast.

[69] The third set of the figure title items contains six pieces of information (superscript NOW) related to the current state of the Dst at that specific epoch. Included are the Dst event size (none, small, medium, or large with thresholds previously defined), its probability of occurrence (1% – 99% scale), source of the forecast (NN = NoNe, SO = Solar Observed event, SP = Solar daily Probability estimate from NOAA, and GP = Geomagnetic daily Probability estimate from NOAA), Xhf flare class and value (C, M, X with the Xhf value appended as a superscript), location of the eruptive event on the solar disk in heliocentric latitude and latitude (N, S and W, E), and speed of the ejecta (km s^{-1}).

[70] Figures 15a and 15b show the Dst effect from two EFRs arising out of two closely spaced erupting events starting at 19 January 2012 centered around 1500 UT. The first Xhf event (A^{X166}) during the 1 h (operationally constrained) interval 19 January 2012 1400 UT (reported the next hour in the 1500 UT time frame) with a location of N34E27 (45° radius from sub-Earth at −30° azimuth) produced an EFR with a calculated velocity of 568 km s^{-1} resulting in a medium size Dst event (A^{D-49}). The second Xhf event (B^{X179}) during 19 January 2012 1500 UT (reported in the 1600 UT time frame) with a location of N34E27 (45° radius from sub-Earth at −30° azimuth) was a continuation of the first event but had grown larger; the event produced an EFR with a calculated velocity of 623 km s^{-1} resulting in a medium size Dst event (B^{D-49}).

[71] Figures 15c and 15d show the 12 h time step predictions of the first and second events. The graphical location of the erupting event on the Earth-visible solar hemisphere from a North pole perspective is a solid-filled dot if the event occurs in the northern hemisphere. If it occurs in the southern hemisphere, it is an open circle. The dot is sized according to its Xhf value with a redundant Xhf magnitude color coding using the size/color scheme of Figure 4. The EFR arc length is notionally sized according to Xhf class ID where "C" is shortest, "M" is medium, and "X" is longest length. The EFR is color coded by Dst

size (blue = none, green = small, orange = medium, and red = large) and the dot size is redundantly set by the size scheme in Figure 4.

[72] The arrival of the first event A^{X166} was predicted to arrive with the Dst event initiation at 22 January 2012 1700 UT having a minimum Dst peak of −46 nT (NOAA G3) 10 h later at 23 January 2012 0300 UT. The second event was predicted to overtake the first event, arriving earlier at 22 January 2012 1100 UT with a minimum (combined with the first event) Dst peak of −75 nT (NOAA G3) 16 h later also at 23 January 2012 0300 UT. Thus, the second event overtakes the first event, arriving about 6 h earlier but combining to form a larger Dst event of −75 nT. The algorithm saves the separate time series vectors of each separate event then sums them with any previous results to arrive at a new Dst profile. Figure 15e shows the combined superposition of both events after the two EFRs have left the Sun and are enroute to Earth. Figure 15f shows the Dst combined event at the arrival positive phase peak SSC of event B^{D-49} at 22 January 2012 0600 UT (reported 1 h later), which is about 5 h earlier than predicted. We do not yet attempt to refine the arrival time using ACE solar wind information.

[73] The storm proceeds to develop into its main phase, reaching its minimum at 23 January 2012 0300 UT (Figure 15g) just as predicted and based on the superposition of both events. Serendipitously, but unrelated, another eruptive event occurs on the Sun at the time of the Dst minimum (Figure 15h) and creates a third Dst prediction. This event was the smallest of the three and the Xhf event (C^{M200}) during 23 January 2012 0300 UT (reported in the 0400 UT time frame) at a location of N29W22 (39° radius from sub-Earth at 29° azimuth) produced an EFR with a calculated velocity of 1128 km s^{-1} resulting in a small size Dst event (C^{D-34}). Figure 15i shows the arrival positive phase peak SSC of third event C^{D-34} at 24 January 2012 1500 UT (reported 1 h later) during the recovery phases of the combined events A^{D-49} and B^{D-49}. Figure 15j shows the end of the recovery period for all three events.

4.9. Metrics

[74] The *Anemomilos* forecast Dst has been correlated against the actual Dst values for the 2001 and 2005 hourly predictions out to +72 h. Tables 2 and 3 show the results of

Table 3. Dst Forecast to Actual Comparisons for Mar–Sep 2005

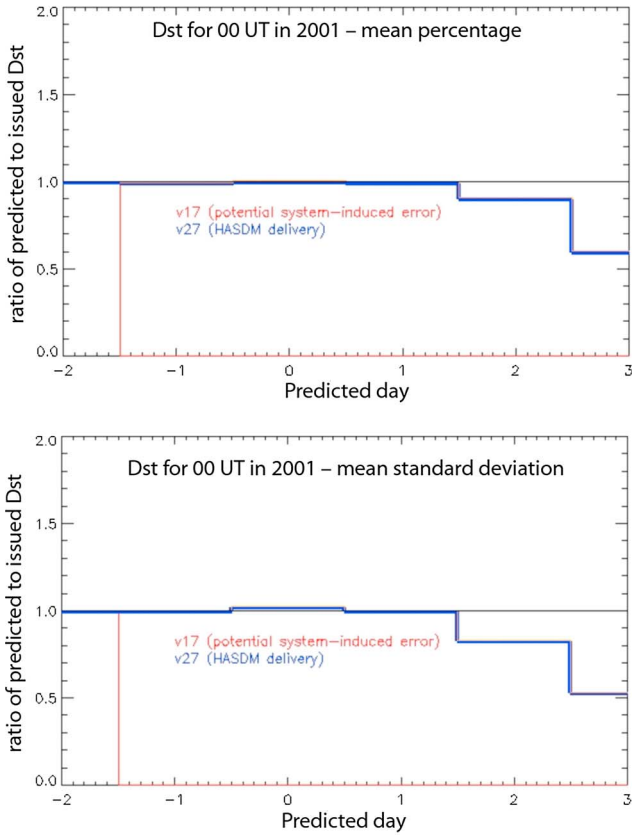| IDX	HR	NowMean	NowSTD	0DyMean	0DySTD	1DyMean	1DySTD	2DyMean	2DySTD	3DyMean	3DySTD
2005	00	1.001	0.999	0.813	1.069	0.777	1.088	0.719	1.015	0.577	0.863
2005	12	1.002	0.999	0.821	1.095	0.758	1.075	0.698	0.982	0.571	0.86

Figure 16. (a) 2001 00 UT mean % ratio. (b) 2001 00 UT 1-σ % ratio.

the forecast compared with the actual Dst using hour-by-hour values in a linear regression correlation. This technique compares initial arrival, main, and recovery phases equally. In both tables are listed the UT hour (HR), mean value percent difference for the Nowcast timeframe (−24 to 0 h, NowMean), the 1-sigma standard deviation (1-σ) for the Nowcast (NowSTD), the current epoch mean value percent difference (0DyMean), 1-σ for the current epoch (0DySTD), 1 day forecast mean value percent difference (+24 h, 1DyMean), 1-σ for the 1 day forecast (1DySTD), 2 day forecast mean value percent difference (+48 h, 2DyMean), 1-σ for the 2 day forecast (2DySTD), and 3 day forecast mean value percent difference (+72 h, 3DyMean), and 1-σ for the 3 day forecast (3DySTD). In each hour epoch example, the mean value, e.g., NowMean, is the simple arithmetic mean (total of the data for all hours in the 2001 or 2005 test period at that hour epoch divided by the number of nonzero elements). The standard deviation is calculated on the mean values so that the 1-σ results can be reported as ratios.

[75] For high solar activity in 2001, the mean of the 1 day predictions for the entire data set are 99% of the actual Dst values, the 2 day predictions are 90%, and the 3 day predictions are 60%. The reason that the 3 day predictions deteriorate is that if there are large Dst events, they tend to arrive earlier than 3 days and these are not predicted;

thus, the prime source of error at 3 days is in the magnitude of the events. For low solar activity in 2005, the values are slightly worse for each of the 3 days although the forecast-to-actual ratios of the 1-σ standard deviations are better than in 2001, i.e., less scatter. It is unclear why this difference occurs and is an area of study.

[76] Figures 16a and 16b as well as Figures 17a and 17b show the Tables 2 and 3 mean value and 1-σ differences for the 00 UT nowcast, current epoch, 1 day, 2 day, and 3 day forecast comparisons in 2001 and 2005. The 12 UT hour plots were similar and are not shown. The blue line is the relevant comparison while the red lines were from reference comparisons not directly related to this discussion.

5. Conclusions

[77] The *Anemomilos* algorithm was developed to serve a unique customer in a specific operational system. It is a redundant capability for forecasting geomagnetic disturbances to the thermosphere and was not designed as a replacement for physics-based models such as ENLIL/Cone/WSA and does not specify parameters that would be expected of those types of models. It does not model nor predict storms resulting from high-speed streams (HSS or CIRs) with origins in coronal holes. It creates forecasts with
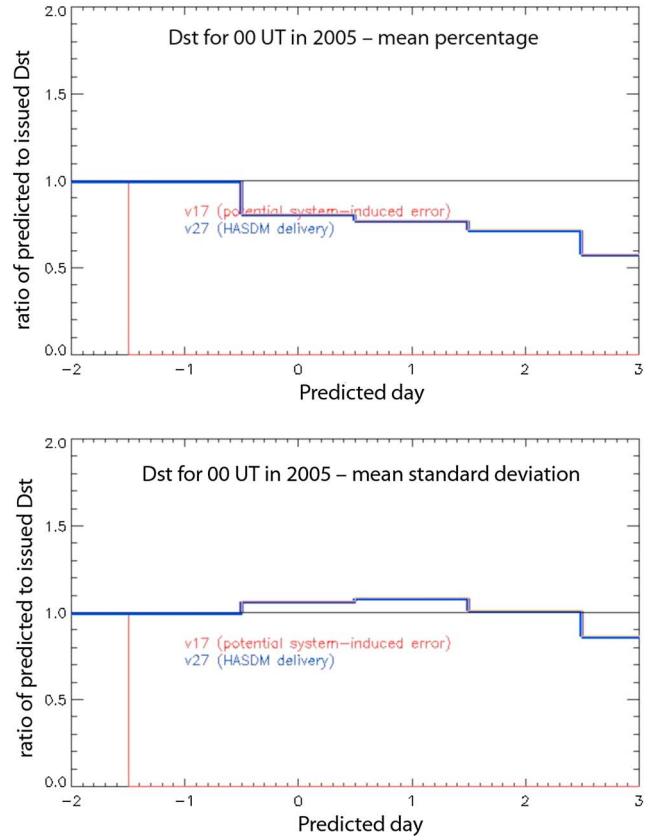

Figure 17. (a) 2005 00 UT mean % ratio. (b) 2005 00 UT 1-σ % ratio.

505

15 min cadence, 1 h time granularity, 144 h prediction window (6 days), and up to 1 h latency. The output forecasts are particularly useful for thermospheric density models such as JB2008 that is used for estimating satellite drag in Low Earth Orbit. The physical basis for *Anemomilos* assumes a relationship between the injected poloidal magnetic flux into solar toroidal flux tubes, the subsequent initiation of an eruption that is observable in 0.1–0.8 nm X-rays with the energetically associated acceleration of eruptive flux ropes off the Sun, and the arrival of the cloud of charged particles at Earth that then affect the main magnetic field, causing a measurable Dst perturbation that is a proxy for high latitude thermospheric heating relevant to operational satellite drag monitoring.

[78] The GOES XRS 0.1–0.8 nm flare flux magnitude, and its integrated light curve, provides a kinetic energy proxy (mass/quantity and speed). It is combined with an IMF connectivity proxy, i.e., the observed solar eruptive event location relative to the solar ecliptic-corrected center of solar disk. The observables enable a deterministic, data-driven forecast of the Dst. The mass/quantity and speed (kinetic energy proxy) observational techniques using the Xhf flare index magnitude and integrated irradiance are described as the erupting event location (IMF connectivity proxy) monitoring technique using the SDO/EVE/SAM observations. Examples of the 19 January 2012 solar flare, EFR, and Dst events are shown.

[79] Linear regression correlations were calculated for every hour of January through July 2001 and March through September 2005 at high and low solar cycle activity. The results indicate that the high solar activity conditions give a slightly better correlation between Dst forecasts and measurements compared with low solar activity for mean value differences and one-sigma standard deviations.

[80] We conclude that *Anemomilos* has been successful because of two factors:

[81] 1. high-level physical processes starting from the Sun and ending at the Earth that create a Dst disturbance are broadly understood; this permits the use of generalized assumptions as the basis for observing proxies for kinetic energy (flare flux magnitude for ejecta mass/quantity and flare integrated irradiance for line-of-sight speed) and IMF connection (erupting event location); these assumptions have allowed us to create inputs to a data-driven, deterministic Dst forecast system; and

[82] 2. operational measurements or proxies for these input drivers are observable, i.e., magnitude and integrated Xhf is the kinetic energy (mass/quantity and speed) proxy and SDO/EVE/SAM flare brightness centroid is the IMF connection (location) proxy; these proxies are available with the regularity and cadence needed for operational users.

[83] We find that nearly all flare events above a certain irradiance magnitude threshold will produce geoeffective charged particle ejecta if they are within a defined solar longitude/latitude region with respect to the solar disk center and if they have sufficient speed. In addition, temporally close, small eruptive events on the Sun can produce separated magnetized solar emissions and these can intermingle on the journey from the Sun to the Earth. Through

the superposition of their energy content, they can create a more significant Dst event at Earth.

[84] Real-time plots of the *Anemomilos* Dst algorithm are updated every 100 s and available for public viewing at the http://sol.spacenvironment.net/~sam_ops/index.html? URL, on the *SpaceWx* smartphone app for iPhones, iPads, and Android devices (icon Magnetosphere: SET-MAG: Dst forecast), and via Twitter feeds that follow either *@spacenvironment* or *#spacewx*. The team plans to make its data available to the scientific community with a time lag of approximately one week. In addition, the team is actively submitting its forecasts to CCMC's "Space Weather Scoreboard." This is an ongoing community metrics study that is independently comparing the results of several CME arrival and magnitude algorithms.

References

Aarnio, A. N., K. G. Stassun, W. J. Hughes, and S. L. McGregor (2011), Solar Flares and Coronal Mass Ejections: A Statistically Determined Flare Flux-CME Mass Correlation, *Sol. Phys., 268,* 195.

Altschuler, M. D., and G. Newkirk (1969), Magnetic fields and structure of solar corona. I. Methods of calculating coronal fields, *Sol. Phys., 9,* 131–149.

Arge, C. N., and V. J. Pizzo (2000), Improvement in the prediction of solar wind conditions using near-real time solar magnetic field updates, *J. Geophys. Res., 105,* 10,465–10,479.

Bak-Steslicka, U., S. Kołomanski, and T. Mrozek (2013), Coronal Mass Ejections Associated with Slow Long Duration Flares, *Solar Phys., 283,* 505–517, doi:10.1007/s11207-013-0251-6.

Barnes, G., K. D. Leka, E. A. Schumer, and D. J. Della-Rose (2007), Probabilistic forecasting of solar flares from vector magnetogram data, *Space Weather, 5,* S09002, doi:10.1029/2007SW000317.

Bhatt, N. J., R. Jain, and A. K. Awasthi (2013), The energetic relationship among geoeffective solar flares, associated CMEs and SEPs, *Res. Astron. Astrophys., 13,* 978–990.

Borovsky, J. E., and M. H. Denton (2006), Effect of plasmaspheric drainage plumes on solarwind/magnetosphere coupling, *Geophys. Res. Lett., 33,* L20101, doi:10.1029/2006GL026519.

Bowman, B. R., W. K. Tobiska, F. A. Marcos, C. Y. Huang, C. S. Lin, W. J. Burke (2008a), A New Empirical Thermospheric Density Model JB2008 Using New Solar and Geomagnetic Indices, AIAA/AAS Astrodynamics Specialist Conference, AIAA 2008–6438.

Bowman, B. R., W. K. Tobiska, F. A. Marcos, and C. Valladares (2008b), The JB2006 empirical thermospheric density model, *J. Atmos. Sol. Terr. Phys., 70,* 774–793.

Burton, R. K., R. L. McPherron, and C. T. Russell (1975), An empirical relationship between interplanetary conditions and Dst, *J. Geophys. Res., 80,* 4204–4214.

Chen, J. (1996), Theory of prominence eruption and propagation: Interplanetary consequences, *J. Geophys. Res., 101*(A12), 27,499–27,519.

Chen, J., and V. Kunkel (2010), Temporal and Physical Connection Between Coronal Mass Ejections and Flares, *Astrophys. J., 717,* 1105–1122, doi:10.1088/0004-637X/717/2/1105.

Chen, A.-Q., and W.-G. Zong (2009), Relationship between CME velocities and X-ray fluxes of associated flares, *Res. Astron. Astrophys.*, *9*, 470–474.

Chen, J., P. J. Cargill, and P. J. Palmadesso (1997), Predicting solar wind structures and their geoeffectiveness, *J. Geophys. Res.*, *102*(A7), 14,701–14,720.

Dungey, J. W. (1961), Interplanetary Magnetic Field and the Auroral Zones, *Phys. Rev. Lett.*, *6*, 47–49.

Emmons, D., A. Acebal, A. Pulkkinen, A. Taktakishvili, P. MacNeice, and D. Odstrcil (2013), Ensemble forecasting of coronal mass ejections using the WSA-ENLIL with CONED Model, *Space Weather*, *11*, 95–106, doi:10.1002/swe.20019.

Falconer, D., A. F. Barghouty, I. Khazanov, and R. Moore (2011), A tool for empirical forecasting of major flares, coronal mass ejections, and solar particle events from a proxy of active-region free magnetic energy, *Space Weather*, *9*, S04003, doi:10.1029/2009SW000537.

Fry, C. D., W. Sun, C. S. Deehr, M. Dryer, Z. Smith, S.-I. Akasofu, M. Tokumaru, and M. Kojima (2001), Improvements to the HAF solar wind model for space weather predictions, *J. Geophys. Res.*, *106*, 20,985–21,001.

Fry, C. D., M. Dryer, C. S. Deehr, W. Sun, S.-I. Akasofu, and Z. Smith (2003), Forecasting solar wind structures and shock arrival times using an ensemble of models, *J. Geophys. Res.*, *108*(A2), 1070, doi:10.1029/2002JA009474.

Gannon, J. L. (2012), Superposed epoch analysis and storm statistics from 25 years of the global geomagnetic disturbance index, USGS-Dst: U.S. Geological Survey Open-File Report 2012–1167.

Gosling, J. T. (1993), The solar flare myth, *J. Geophys. Res.*, *98*(A11), 18,937–18,949.

Harrison, R. A. (1995), The nature of solar flares associated with coronal mass ejection, *Astron. Astrophy.*, *304*, 585–594.

Hoeksema, J. T. (1984), PhD thesis, Stanford University.

ISO 16290 (2012), Definition of the Technology Readiness Levels (TRL) and their criteria of assessment, International Standards Organization, Geneva.

Jackson, B. V., P. Hick, M. Kojima, and A. Yokobe (1998), Heliospheric tomography using interplanetary scintillation observations. 1. Combined Nagoya and Cambridge data, *J. Geophys. Res.*, *103*, 12,049–12,067.

Jain, R., M. Aggarwal, and P. Kulkarni (2010), Relationship between CME dynamics and solar flare plasma, *Res. Astron. Astrophys.*, *10*, 473.

Kahler, S. W. (1992), Solar Flares and Coronal Mass Ejections, *Ann. Rev. Astron. Astrophys.*, *30*, 113–141.

Knipp, D., S. Eriksson, L. Kilcommons, G. Crowley, J. Lei, M. Hairston, and K. Drake (2011), Extreme Poynting flux in the dayside thermosphere: Examples and statistics, *Geophys. Res. Lett.*, *38*, L16102, doi:10.1029/2011GL048302.

Lanzerotti, L. J. (2012), Small Businesses and Space Weather Products, *Space Weather*, *10*, S02010, doi:10.1029/2012SW000774.

Li, W., D. Knipp, J. Lei, and J. Raeder (2011), The relation between dayside local Poynting flux enhancement and cusp reconnection, *J. Geophys. Res.*, *116*, A08301, doi:10.1029/2011JA016566.

Lionello, R., J. A. Linker, and Z. Mikic (2001), Including the transition region in models of the large-scale solar corona, *ApJ*, *546*(1), 542, doi:10.1086/318254.

Lopez, R. E., R. Bruntz, E. J. Mitchell, M. Wiltberger, J. G. Lyon, and V. G. Merkin (2010), Role of magnetosheath force balance in regulating the dayside reconnection potential, *J. Geophys. Res.*, *115*, A12216, doi:10.1029/2009JA014597.

Love, J. J., and J. L. Gannon (2010), Movie-maps of low-latitude magnetic storm disturbance, *Space Weather*, *8*, S06001, doi:10.1029/2009SW000518.

Luhmann, J. G., Y. Li, C. N. Arge, P. R. Gazis, and R. Ulrich (2002), Solar cycle changes in coronal holes and space weather cycles, *J. Geophys. Res.*, *107*(A8), 1154, doi:10.1029/2001JA007550.

Lyon, J. G., J. A. Fedder, and C. M. Mobarry (2004), The Lyon-Fedder-Mobarry (LFM) global MHD magnetospheric simulation code, *J. Atmos. Sol. Terr. Phys.*, *66*, 1333–1350.

Mayaud, P. N. (1980), *Derivation, Meaning, and Use of Geomagnetic Indices*, Geophysical Monograph, vol. 22, American Geophysical Union, Washington D.C.

Merkin, V. G., and J. G. Lyon (2010), Effects of the low-latitude ionospheric boundary condition on the global magnetosphere, *J. Geophys. Res.*, *115*, A10202, doi:10.1029/2010JA015461.

Mertens, C. J., W. K. Tobiska, D. Bouwer, B. T. Kress, M. J. Wiltberger, S. C. Solomon, and J. J. Murray (2009), Development of Nowcast of

Atmospheric Ionizing Radiation for Aviation Safety (NAIRAS) model, AIAA 2009–3633, 1st AIAA Atmospheric and Space Environments Conference, San Antonio, Texas.

Mikic, Z., J. A. Linker, D. D. Schnack, R. Lionello, and A. Tarditi (1999), Magnetohydrodynamic modeling of the global solar corona, *Phys. Plasmas*, *6*(5), 2217.

Mulligan, T., C. T. Russell, and J. G. Luhmann (1998), Solar cycle evolution of the structure of magnetic clouds in the inner heliosphere, *Geophys. Res. Lett.*, *25*(15), 2959–2962.

NASA/TM—2006–214137 (2006), Solar Sentinels: Report of the Science and Technology Definition Team, Goddard Space Flight Center, Greenbelt, Maryland 20771.

Newell, P. T., T. Sotirelis, K. Liou, C.-I. Meng, and F. J. Rich (2007), A nearly universal solar wind-magnetosphere coupling function inferred from 10 magnetospheric state variables, *J. Geophys. Res.*, *112*, A01206, doi:10.1029/2006JA012015.

O'Brien, T. P., and R. L. McPherron (2000), Forecasting the ring current Dst in real time, *J. Atmos. Sol. Terr. Phys.*, *62*, 1295–1299.

Odstrčil, D., and V. Pizzo (1999), Three-dimensional propagation of coronal mass ejections (CMEs) in a structured solar wind flow 1. CME launched within the streamer belt, *J. Geophys. Res.*, *104*(A1), 483–492.

Odstrcil, D., P. Riley, and X. Zhao (2004), Numerical simulation of the 12 May 1997 interplanetary CME event, *J. Geophys. Res.*, *109*, A02116, doi:10.1029/2003JA010135.

Perreault, P., and S.-I. Akasofu (1978), A study of geomagnetic storms, *Geophys. J. R. Astron. Soc.*, *54*, 547–573.

Pizzo, V., G. Millward, A. Parsons, D. Biesecker, S. Hill, and D. Odstrcil (2011), Wang-Sheeley-Arge–Enlil cone model transitions to operations, *Space Weather*, *9*, S03004, doi:10.1029/2011SW000663.

Raeder, J., Y. Wang, and T. Fuller-Rowell (2001), Geomagnetic Storm Simulation With a Coupled Magnetosphere-Ionosphere-Thermosphere Model, in *Space Weather: Progress and Challenges in Research and Applications*, Geophysical Monograph, vol. 125, edited by P. Song et al., pp. 377–384, AGU, Washington, D.C.

Reames, D. V. (2002), Magnetic topology of impulsive and gradual solar energetic particle events, *Astrophys. J.*, *571*, L63–L66, doi:10.1086/341149.

Riley, P., J. A. Linker, and Z. Mikic (2001), An empirically-driven global MHD model of the corona and inner heliosphere, *J. Geophys. Res.*, *106*(A8), 15,889–15,901.

Riley, P., J. A. Linker, and Z. Mikic (2002), Modeling the heliospheric current sheet: Solar-cycle variations, *J. Geophys. Res.*, *107*(A7), 1136, doi:10.1029/2001JA000299.

Schatten, K. H., J. M. Wilcox, and N. F. Ness (1969), A model of interplanetary and coronal magnetic fields, *Sol. Phys.*, *6*, 442–455.

Shimojo, M., and K. Shibata (2000), Physical parameters of solar X-ray jets, *Astrophys. J.*, *542*, 1100–1108.

Sugiura, M., and S. Hendricks (1967), Provisional hourly values of equatorial Dst for 1961, 1962 and 1963, NASA Tech. note D-4047, Goddard Space Flight Center, Greenbelt, MD.

Temerin, M., and X. Li (2002), A new model for the prediction of Dst on the basis of the solar wind, *J. Geophys. Res.*, *107*(A12), 1472, doi:10.1029/2001JA007532.

Tobiska, W. K. (2003), Forecast E10.7 for Improved LEO Satellite Operations, *J. Spacecraft Rock.*, *40*(3), 405–410.

Tobiska, W. K., and S. D. Bouwer (2006), New developments in SOLAR2000 for space research and operations, *Adv. Space Res.*, *37*(2), 347–358, doi:10.1016/j.asr.2005.08.015.

Tobiska, W. K., S. D. Bouwer, and B. R. Bowman (2008), The development of new solar indices for use in thermospheric density modeling, *J. Atmos. Sol. Terr. Phys.*, *70*, 803–819.

Toffoletto, F. R., S. Sazykin, R. W. Spiro, and R. A. Wolf (2003), Modeling the Inner Magnetosphere using the Rice Convection Model (review), *Space Sci. Rev.*, WISER special issue, *108*, 175–196.

Török, T., and B. Kliem (2005), Confined and Ejective Eruptions of Kink-unstable Flux Ropes, *Astrophys. J.*, *630*, L97–L100.

Tóth, G., et al. (2005), Space Weather Modeling Framework: A new tool for the space science community, *J. Geophys. Res.*, *110*, A12226, doi:10.1029/2005JA011126.

Tsyganenko, N. A. and M. I. Sitnov (2005), Modeling the dynamics of the inner magnetosphere during strong geomagnetic storms, *J. Geophys. Res.*, *110*, A03208, doi:10.1029/2004JA010798.

Tsyganenko, N. A. and M. I. Sitnov (2007), Magnetospheric configurations from a high-resolution data-based magnetic field model, *J. Geophys. Res.*, *112*, A06225, doi:10.1029/2007JA012260.

Valdivia, J. A., A. S. Sharma, and K. Papadopoulos (1996), Prediction of magnetic storms by nonlinear models, *Geophys. Res. Lett.*, *23*(21), 2899–2902.

Vršnak, D., D. Ruždjak, B. Sudar, and N. Gopalswamy (2004), Kinematics of coronal mass ejections between 2 and 30 solar radii: What can be learned about forces governing the eruption?, *Astron. Astrophys.*, *423*, 717–728.

Wang, Y. M., and N. R. Sheeley (1992), On potential-field models of the solar corona, *Astrophys. J.*, *392*(1), 310–319 Part 1.

Wolf, R. A., R. W. Spiro, and F. J. Rich (1991), Extension of the Rice Convection Model into the high-latitude ionosphere, *J. Atmos. Terr. Phys.*, *53*, 817–829.

Yashiro, S., and N. Gopalswamy (2009), Statistical relationship between solar flares and coronal mass ejections, in *IAU Symposium*, vol. 257, edited by N. Gopalswamy and D. F. Webb, pp. 233–243, Universal Heliophysical Processes, Cambridge Univ. Press, London.

Yashiro, S., S. Akiyama, N. Gopalswamy, and R. A. Howard (2006), Different Power-Law Indices in the Frequency Distributions of Flares with and without Coronal Mass Ejections, *Astrophys. J. Lett.*, *650*, L143–L146.

Zhang, J., K. P. Dere, R. A. Howard, M. R. Kundu, and S. M. White (2001), On the temporal relationship between coronal mass ejections and flares, *Astrophys. J.*, *559*, 452–462.